Structural and property engineering of 2D titanium carbides (MXene) thin films using ion irradiation

Ayoub Benmoumen, Marie-Laure David, Eric Gautron, Simon Hurand, Sophia Tangui, Lola Loupias, Aurélien Habrioux, Stéphane Célérier, Philippe Moreau, Vincent Mauchamp

Structural and Property Engineering of 2D Titanium Carbides (MXene) Thin Films Using Ion Irradiation.

Ayoub Benmoumen, Marie-Laure David*, Eric Gautron, Simon Hurand, Sophia Tangui, Lola Loupias, Aurélien Habrioux, Stéphane Célérier, Philippe Moreau* and Vincent Mauchamp*

A. Benmoumen, Dr. M-L. David, Dr. S. Hurand, Sophia Tangui, Prof. V. Mauchamp
Université de Poitiers, CNRS, ISAE-ENSMA, PPRIME, Poitiers, France
E-mail : marie-laure.david@univ-poitiers.fr; vincent.mauchamp@univ-poitiers.fr

A. Benmoumen, Dr. Eric Gautron, Prof. P. Moreau
Nantes Université, CNRS, Institut des Matériaux de Nantes Jean Rouxel, IMN, F-44000 Nantes, France
E-mail : Philippe.moreau@cnrs-imn.fr

Dr. Lola Loupias, Dr. A. Habrioux, Dr. S. Célérier,
Université de Poitiers, CNRS, IC2MP,
B27 4 rue Michel Brunet, 86073 Poitiers, France

Keywords: MXenes, Ion irradiation, STEM-EELS, optical properties, electrical properties, thin films

Abstract

MXenes are a large family of two-dimensional transition metal carbides and/or nitrides combining hydrophilicity with metallic conductivity, thereby leading to a plethora of potential applications. This study expands the current possibilities for the structural engineering of MXenes by demonstrating medium energy range ion irradiation as a controllable and flexible strategy to deeply modify $Ti_3C_2T_z$ thin films. By adjusting the fluence of a 180 kV He^+ ion beam, we evidence the gradual modification of the different structural elements of typical MXene multilayers, inducing well-defined impacts on properties. Low fluences allow modifying the interlayer spacing, inhibiting the long-term rehydration capacity of the thin films with expected major benefits on MXene aging issues. In addition to this, irradiation allows affecting the layers functionalization with major impact on the normalized optical transmission profile, suppressing the absorption valley at IR-visible limit and expanding their transparency in the UV. These effects, combined with improved electrical contact between the $Ti_3C_2T_z$ layers, are highly desirable for transparent conductive electrodes applications. Finally, higher fluence irradiations induce preferential sputtering of titanium atoms. Transition metal vacancies

being known to be highly relevant to deeply modify properties beyond those investigated here, these results show the large benefits of ion irradiation for MXene design.

1. Introduction

Two-dimensional (2D) transition metal carbides or nitrides, known as MXenes [1], are quite unique in the very diverse world of 2D materials. Among other reasons is the fact that, contrary to many other 2D systems, which are either semimetals [2], semiconductors [3] or insulators [4], many MXenes exhibit an outstanding metallic behavior [5,6]. As an example, a conductivity of 24000 $S.cm^{-1}$ was recently reported for $Ti_3C_2T_z$, the most studied MXene to date [7]. In addition, MXene 2D layers exhibit tunable hydrophilicity and easy dispersion in water without surfactant, enabling scalable, flexible, and cost-effective processing as thin films, inks or membranes [8,9]. For this unique combination of properties, they are heavily investigated for an ever increasing range of applications including electromagnetic interference shielding [10], sensing [11], or energy storage and conversion [12]. In particular, the combination of the above-mentioned properties with good transparency [13] and tunable work function [14] offers very exciting perspectives in optoelectronic applications for MXene thin films [15], including charge transport layers (CTL) or transparent conductive electrodes (TCE) in photovoltaic cells [16,17], light emitting diodes [18], photodetectors [19,20] or transparent supercapacitors [21,22].

Another true originality pushing forward MXene development is their high chemical and structural diversity. More than 40 different compounds have been synthesized to date [23], offering large opportunities in changing their properties. Being obtained from the chemical exfoliation of the A element (*e.g.* Al, Si) from MAX phases [24], a more than 150 members family of nanolaminated ceramics with $M_{n+1}AX_n$ chemical formula (M being a transition metal, X being either C or N, and n = 1 to 4), one can change the nature of the M and X elements or the intrinsic thickness of MXene layers (*i.e.*, varying n) by using different MAX phase precursors. This has a major impact in terms of physico-chemical properties [25–28]. Besides, one can also play with MXenes surface functionalization, inherited from the MAX phase exfoliation step usually involving quite harsh acidic conditions [29]. This leads to the following chemical composition for the MXene 2D layers: $M_{n+1}X_nT_z$ with the T surface groups being, *e.g.* F, O, OH and/or Cl, and z being usually close to 2. Because they are directly bonded to the M element - the *d*-bands of which dominate the electronic structure at the Fermi level -, controlling the T-groups has also been shown as a relevant strategy to modify MXenes properties [30–33].

Finally, properties modulations can also be achieved through molecular grafting or intercalation in multilayers, unveiling the superior flexibility that one can achieve in MXene structural richness [34–36].

However, an ultimate way of driving MXenes chemistry would be to shift from properties modification to properties optimization. In this context, first principles calculations show that such an optimization is non-trivial to obtain [37,38]: it is achieved for well-defined substitution levels on the different atomic sites (depending on the type of MXene and investigated properties) and can be highly challenging to control from the synthesis point of view. From this perspective, ion beam techniques are extremely relevant physical approaches allowing the chemical and structural engineering of materials thanks to a perfect control over the ion beam characteristics (fluence, energy, type of ions) used to modify the material [39], and providing significant advantages: high reproducibility, doping possibilities with almost all elements from the periodic table, possibility to obtain original structures beyond thermodynamic limits, and fine tunability of the doping/damage rate (*i.e.*, density of defects, dopants, etc.). Experimental adjustments to optimize properties for targeted applications are consequently made possible. This later point is of utmost importance since such optimization often require a trade-off between different, and sometimes antagonistic, properties such as electrical conductivity and optical transparency regarding TCE. Ion beam approaches have been successfully explored since more than a decade in different types of 2D materials [40,41] with great success in, *e.g.*, improving the elastic modulus of graphene [42], improving gas permeation or gas sensing in graphene [43,44], or tuning the optical properties of WS_2 [45]. These techniques are still very scarcely used for effective properties tuning strategies in MXenes, and only focusing on ion implantation [46,47], despite recent results showing that $Ti_3C_2T_z$ thin films are very interesting 2D platforms for ion beam defect engineering due to their high damage tolerance [48].

In the present study, and focusing on $Ti_3C_2T_z$ spin-coated thin films, ion irradiation is shown to be an effective strategy to perform structural engineering in MXenes layers. A major impact on their properties is demonstrated, focusing on some of their most salient characteristics: their hydrophilicity and optoelectronic properties. By combining different structural/chemical characterization approaches (*e.g.* White Light Interferometry -WLI-, X ray diffraction -XRD-, and advanced Transmission Electron Microscopy -TEM) with optical and electrical ones (*e.g.* Variable Angle Spectroscopic Ellipsometry -VASE), we show that one can take advantage of the different sensitivity to ion irradiation of the M, X and T elements [49,50],

as well as of the intercalated species (ions, water), in the $Ti_3C_2T_z$ multilayers. This allows to gradually modify the structure and chemistry of the thin films by carefully adjusting the fluence of a medium energy He^+ ion beam in a step by step procedure. At low fluence, a metastable to stable modification of the interlayer species can be achieved with the removal of the intercalated water in between MXene layers and significant inhibition of the hydration ability of the thin films over a long time scale. This is a key point for the long-term stability of MXene-based electrodes where confined water induces the hydrolysis of their surface, leading to their degradation [51,52]. In the same fluence range, the surface functionalization of the layers can be modified. This leads to the suppression of the transmittance valley observed at the onset of the visible range, ascribed to a surface plasmon resonance [25,27], and leading to an homogeneous transmission profile in the corresponding energy range. Finally, increasing the He^+ fluence allows deep modifications of the MX core with Ti preferential sputtering, thus providing a complete structural manipulation of the MXene stack.

2. Material and methods

2.1 MXene thin film preparation

$Ti_3C_2T_z$ thin films were prepared by spin coating of an aqueous solution (50 $mg.mL^{-1}$) of delaminated MXene powder synthetized from Ti_3AlC_2 precursor following the protocol detailed in [48], on top of a 1×1 cm^2 quartz substrate. The aqueous solution was prepared through a simple hand-shaking of a water suspension of the MXene powder for 10 minutes, followed by sonication for 20 minutes. The thin films were then deposited using a Polos SPIN150i/200i spin coater at room temperature to achieve thicknesses ranging from 50 nm to 150 nm.

2.2 Ion Implantation

The MXene thin film samples were mounted on a sample holder and exposed to an ion beam directed perpendicularly to the substrate. They were exposed to 180 keV He^+ ions with a probe current of 10 µA under high vacuum chamber of about 5×10^{-7} mbar at room temperature. Implantations were performed at four different ion fluences: 3×10^{15}, 8×10^{15}, 1.5×10^{16} and 7×10^{16} $ions.cm^{-2}$. The damage and ion distribution depth profiles calculations were performed using Stopping and Range of Ions in Matter (SRIM) [60], with an estimated $Ti_3C_2T_z$ thin film density of 4.26 $g.cm^{-3}$ considering a *c* parameter of 19.6 Å and a mixture of O/F terminations. The (default) displacement energies used were 25 eV for Ti, 28 eV for C, 28 eV for O and 25 eV for F. The number of created vacancies were obtained using detailed calculations with full damage cascade method. MXene multilayers are however intrinsically not dense materials and

considering that the films are porous, the corresponding SRIM results are expected to be indicative in nature, not quantitative. They were nevertheless shown to give a good estimation of the ion distribution profile for Mn^+ implantation in $Ti_3C_2T_x$ by H. Pazniak *et. al* [48].

2.3 Thin film characterization

Thickness measurements were systematically performed on the samples by White Light Interferometry (WLI) using a Taylor Hobson Precision Talysurf CCI 6000. A small scratch was performed in the center of the sample (see Figure 1-d) using a needle with a micrometric tip. The step height was averaged over a region of several hundreds of micrometers. The very same step is used before and after irradiation in order to reveal possible irradiation-induced sputtering.

The XRD patterns obtained for the $Ti_3C_2T_z$ thin films, before and after irradiation, were measured in air, at room temperature using a Bruker D8 diffractometer in Bragg Brentano geometry, with a Cu K_α radiation (1.5406 Å) at U = 40 kV and I = 40 mA, from 5° to 70° with a step size of 0.025° and a dwell time of 1 s/step.

Resistivity measurements were performed at room temperature using the van der Pauw method, and an ECOPIA HMS-5000 equipment.

The dielectric functions of the samples were characterized using Variable Angle Spectroscopic Ellipsometry (VASE) in the NIR-vis-UV range (0.7 – 5.9 eV, corresponding to a 1687 - 211 nm wavelength range) using a J. A. Woollam M2000X, which was also used in transmission intensity mode for the transmission measurements. The ellipsometric angles Ψ and Δ were collected at incident angles of 45°, 55°, 65° and 75°. The resulting data were then analyzed using the CompleteEase software supported by the J. A. Woolam Company. The optical models used to fit the data are described in detail in the Supporting Information (part S1).

The TEM samples were prepared by scratching the thin film surface using a razor blade or a diamond tip to peel the $Ti_3C_2T_z$ flakes, and then sweeping them out using a Cu grid covered with a lacey carbon film. The MXene flakes were probed using a Cs-probe corrected Themis Z G3 (Thermo Fisher Scientific) Scanning Transmission Electron Microscope (S/TEM), operated at 300 kV accelerating voltage. Electron Energy-Loss Spectroscopy spectrum imaging (EELS-SI) was performed in microprobe mode with a 0.69 mrad convergence angle, a 3.6 mrad collection angle and a probe size of 3.2 nm full width at tenth maximum. Such low convergence angle allows minimizing the electron dose, calculated to be 1.2 10^5 $e^-/Å^2$, using a probe current around 150 pA. The current and the exposition time were chosen in such a way as to prevent the sample from electron beam degradation: no evolution of the samples morphology or chemistry was observed during the acquisitions, in agreement with recently published

simulations showing that the overall surface composition of $Ti_3C_2T_z$ MXene flakes should not be altered in such conditions [50]. Spectra were recorded on a GIF Quantum ERS 966 spectrometer (Gatan), equipped with a K2 Summit direct electron detection camera (Gatan) and a US1000 CCD camera. The data were acquired using the DUAL-EELS mode using the CCD camera at a dispersion of 0.25 eV/pixel with a current ≈ 150 pA, allowing for the simultaneous acquisition of the low loss and core loss spectra for the deconvolution of multiple scattering effects related to thickness variations. Core edges were extracted from the background using a power law. The spectra shown in figures 3-a,b and 4-a,b present an average of several spectra measured for a given sample, except for the one irradiated at 7×10^{16} ions.cm^{-2}, where the spectra collected from four different areas are presented because they present a markedly different level of damage. EEL spectra were collected in areas of thicknesses over inelastic mean free path ratios, t/λ, ranging from ~ 0.2 to 0.4. In order to improve the visibility and comparability of the spectra, they were all normalized at the Ti-L_2-edge's tail at 469 eV and calibrated using the carbon K-edge energy at 285 eV, proven to be constant in all samples.

The cross section TEM lamella was prepared and extracted from the sample by a dual beam FIB tool (Helios CX G3 From Thermofisher Scientific) and was transported to the TEM instrument via a conventional TEM Molybdenum half-grid. The preliminary thinning process under the Ion beam (Ga^+) was performed at 30 kV and currents dropping from 0.43 nA to 80 pA as a function of the lamella thickness. When reaching the desired thickness, the process was terminated with two cleaning steps: the first at 5 kV and 15 pA along both sides of the foil, and the final step at 2 kV and 9 pA again on each side of the foil. The lamella was then polished by a Precise Ion Polisher II (PIPSII-Gatan) using an Ar beam at 500 V, 3 rpm, 5 degrees and a modulation angle of 20 degrees. The cross section was then probed using a JEOL 2200 FS microscope, operated at 200 kV in both STEM and HR-TEM modes.

3. Results and discussion

3.1 Pristine $Ti_3C_2T_z$ thin film characterization

$Ti_3C_2T_z$ MXene powders were obtained *via* a LiF + HCl etching protocol of the Al layers from the Ti_3AlC_2 parent MAX phase [53]. Powders were then prepared as colloidal suspensions for spin-coating on quartz substrates (see the methods section). The initial pristine powders present typical delaminated MXene flakes with regular shapes and sizes of a few µm² [54] as evidenced in Figure 1-a where a TEM micrograph of a typical stack of a few MXene flakes is shown. The corresponding electron diffraction pattern (see inset) shows the expected hexagonal structure

inherited from the parent MAX phase Ti_3AlC_2 [53]. No sign of oxidation is observed. This would show up as extra spots or diffuse rings at shorter distances. The chemical composition of the $Ti_3C_2T_z$ flakes was studied by Electron Energy Loss Spectroscopy (EELS), a typical spectrum being given in Figure 1-b. It clearly shows the C K and Ti $L_{2,3}$-edges from which a Ti/C ratio of ~ 1.5 ± 0.04 was obtained, in agreement with the expected composition. In addition, the presence of the typical surface terminations induced by the LiF/HCl exfoliation protocol is also clearly evidenced in the EEL spectra with the Cl $L_{2,3}$, O K and F K-edges (see the structural model in inset). The fine structures at these different edges are fully consistent with previously published data for the $Ti_3C_2T_z$ system [54–56]. In particular, given the sensitivity of the C K-edge to the surface chemistry and defects in the MXene layers [54], these data confirm the good quality of the samples.

After spin-coating, the MXene sheets stack up parallel to the substrate surface, creating thin films of typical thicknesses ranging from 50 to 150 nm, as measured by WLI (see Figure 1-d). This stacking is shown in the cross-sectional High Angle Annular Dark Field (HAADF) - Scanning TEM (STEM) micrographs given in Figures 1-c and e. These films appear to be somewhat porous. Elongated pores are visible as dark contrasts in Figure 1-c and e (circled in white). The surface roughness of the film is in the order of 30 nm, as measured by WLI, in agreement with cross-section TEM observations. Besides these points, the MXene flakes are very well aligned in the thin film as evidenced in Figure 1-f. The X ray diffractograms recorded on the thin films, and given in SI (Part S2), are characteristic of wet multilayer stackings with a (002) peak around 7°, significantly shifted as compared to the MAX phase, and with hardly distinguishable higher order (00l) reflections [57]. These XRD data also show a very small quantity of unreacted MAX phase remaining in the present film, way too small to influence any of the here-discussed results. One should notice that such MAX phase residual was not detectable in the XRD data of the powders used to elaborate the films (see SI part S2, Figure S2b), and is not present on all the investigated films. It is probably due to the redispersion of isolated un-etched grains when preparing the solution for spin-coating. The fact that the LiF-HCl method is not as efficient as concentrated HF for MAX phase etching has been evidenced using Nuclear Magnetic Resonance by different authors [58,59]. However, it is better suited to produce stable colloidal suspensions, used as the starting material for the thin films elaboration, than concentrated HF which requires additional steps (insertion of organic molecules, ultrasonication etc.).

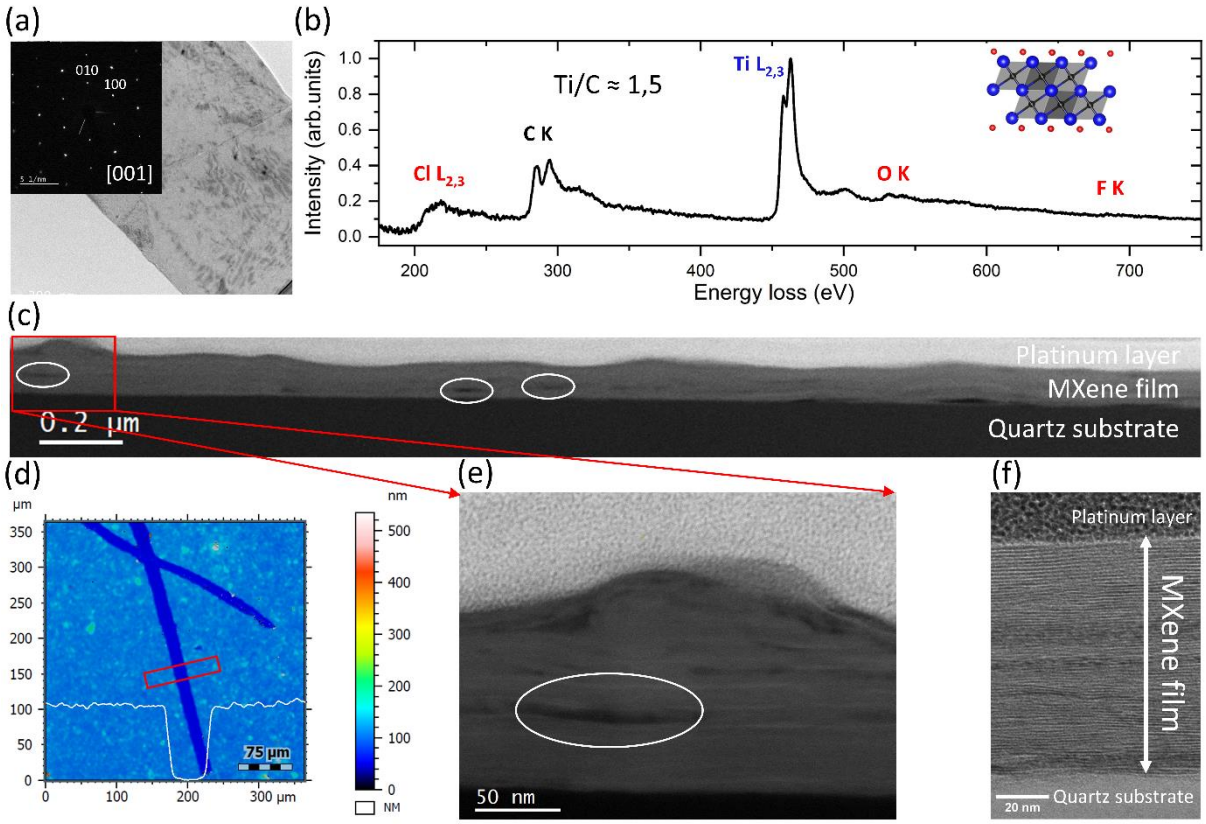

Figure 1: (a) TEM micrograph of a $Ti_3C_2T_z$ MXene flake, with the corresponding energy filtered Selected Area Electron Diffraction (SAED) pattern (inset). (b) Typical spliced STEM-EEL spectrum of a $Ti_3C_2T_z$ sample showing the Cl $L_{2,3}$, C K, Ti $L_{2,3}$, O K and F K-edges. A schematic structure of a $Ti_3C_2T_z$ sheet is also given: titanium atoms are represented in blue, carbon atoms in black, and surface groups in red. (c) Cross-sectional HAADF-STEM micrograph of a FIB prepared MXene thin film, the porosities in the sample are circled in white. (d) WLI image of a sample surface showing the scratch used to measure the thickness. The thickness is about 100 nm in the present case, as shown from the superimposed thickness profile obtained by averaging over multiple lines (the red rectangle). (e) Higher magnification STEM-HAADF micrograph of the area highlighted by a red square in figure (c). (f) High resolution TEM micrograph of the thin film.

3.2 Structural engineering by ion irradiation

Structural engineering in the $Ti_3C_2T_z$ thin films was performed using He^+ ion irradiation at 180 keV. According to Stopping and Range of Ions in Matter (SRIM) calculations [60], this irradiation condition produces homogeneous, *i.e.* flat, ion damage profiles in the $Ti_3C_2T_z$ thin films over the desired thickness (< 200 nm), with most of the ions passing through the MXene film and being implanted into the quartz substrate (see SI – Part S3). All details concerning SRIM calculations are given in the methods section. The implantations were conducted at four different fluences, 3 x 10^{15}, 8 x 10^{15}, 1.5 x 10^{16} and 7 x 10^{16} ions.cm^{-2}, gradually increasing the amount of structural defects introduced into the samples. Each implantation has been reproduced typically on three to six different thin films in order to assess the reproducibility of the results. Henceforth, these irradiated samples will be referred to as **S3**, **S8**, **S15** and **S70**, respectively. These different fluences were chosen to gradually modify the MXene structure by

playing on different structural levels, which are expected to behave differently under ion irradiation. The intercalated interlayer water molecules and cations are expected to be the most irradiation sensitive species, followed by the surface groups and finally the M-X skeleton, which should be more damage tolerant, each one of these units having its own role on MXene properties [26,30,61].

Before going into the detailed characterization of the irradiation-induced structural damages in the MXene layers, we discuss the impact on the organization of the layers at the thin film scale. We first focus on water interlayer confinement as probed using XRD with particular attention paid to the (002) reflection. This peak reflects the sheet stacking and spacing, described by the *c* lattice parameter as shown in the structural model in Figure 2-a. It is indeed well established that this signature is highly sensitive to water intercalation between the MXene layers, stabilized by the surface groups and intercalated cations coming from the etchant (Li^+ in the present case) [61,62]. From a quantitative analysis of *in-situ* XRD data, S. Célérier *et al.* [61] showed that the (002) angular position allows for the identification of the intercalation of a single layer (1WL), double layer (2WL) or the absence (0WL) of water molecules between the $Ti_3C_2T_z$ layers, this phenomenon being highly sensitive to the ambient atmosphere relative humidity and determined by the hydrophilic character induced by the surface functionalization of the MXene layers. XRD measurements, focusing on the (002) peak region, were thus performed on the pristine and irradiated samples (immediately following the irradiation) as shown in Figure 2-b. The expected positions for the (002) peak corresponding to the 0WL, 1WL and 2WL situations are also reported as blue rectangles. As seen, irradiation appears to have a strong effect on the interlayer spacing of the MXene films. The pristine sample presents a strong peak at $2\theta = 7.08°$, corresponding to a ~25 Å *c* parameter and thus 1WL, with a small shoulder around 6.2° indicating the coexistence of a small portion of 2WL, partially distributed among the 1WL and reflecting the interstratification and segregation phenomena at stake [61]. The S3 sample, *i.e.* corresponding to the lowest fluence, shows a markedly different XRD pattern: it appears to be made up of 3 overlapping peaks, one between 2WL and 1WL at 6.1°, a larger one around the 1WL level and finally a third one between 1WL and 0 WL. According to the analysis of S. Célérier *et al.*[61], this is due to a random mixture of the three states, creating a large diffraction signal caused by the varying interlayer distances along the sample. All other irradiated samples present a single peak between 1WL and 0 WL, with a decreasing *c* from ~23 Å for S8 to ~22 Å for S70. It should be noted here that the XRD do not change at higher 2θ values under He^+ irradiation, no phase transformation being observed at this scale.

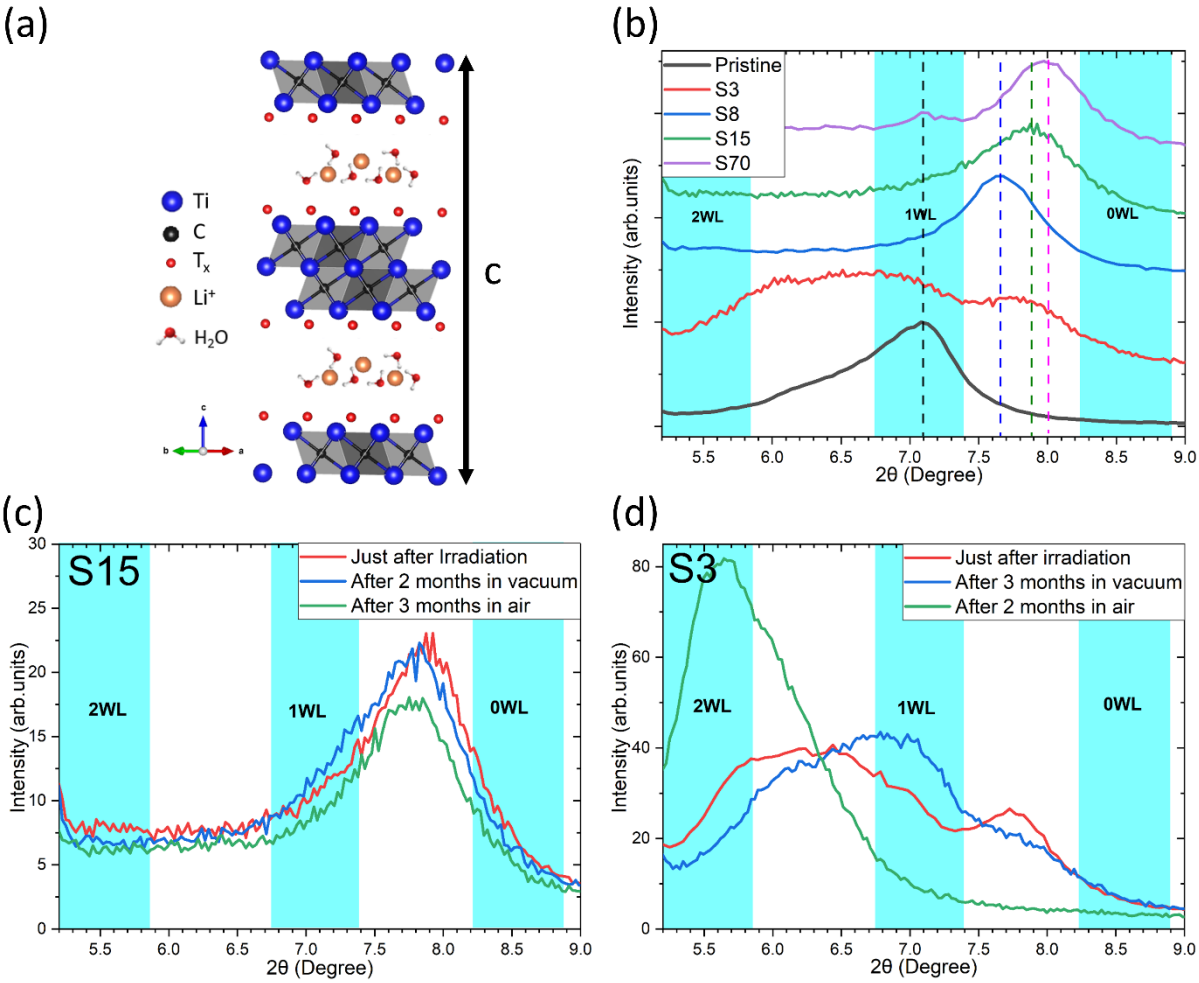

Figure 2: (a) Schematic representation of a $Ti_3C_2T_z$ multilayer stack showing the intercalated water molecules stabilized by Li^+ ions along with the **c** parameter. (b) Typical X-ray diffractograms of the pristine and irradiated samples showing the evolution of the (002) peaks with respect to the irradiation fluence. The expected positions of this peak for 0, 1 and 2 water layers (WL) intercalated between the MXene sheets are also indicated as blue areas following the results of S. Célérier et al [61]. Diffractograms were normalized and shifted vertically to ease comparison. (c,d) X-ray diffractograms showing the aging of the S15 and S3 samples (respectively) under low vacuum and then in air.

These results indicate a clear and gradual modification of the interlayer spacing with irradiation due to intercalated water layer and cations removal. More importantly, the dehydrated states obtained after irradiation at fluences greater than 3.10^{15} ions.cm^{-2} are very stable since XRD patterns recorded after storing the samples for two months in low vacuum and three further months at ambient atmosphere show no evolution (see Figure 2-c for S15), meaning that the films did not rehydrate. On the contrary, the S3 irradiated thin film (Figure 2-d) showed a marked rehydration after similar aging with a main (002) peak corresponding to the coexistence of 1WL and 2WL. This clearly highlights the ability of ion irradiation to gradually modify MXene structure starting from a metastable modification of the interlayer spacing of sample S3 before going to a stable state, for higher fluences, where the ability of the $Ti_3C_2T_z$ layers to rehydrate is very significantly reduced. It is consistent with the increased hydrophobic character

observed on exfoliated Ti_3SiC_2 powders just after low energy N^+ implantation [47]. This result is especially important regarding the environmental stability of MXenes and corresponding MXene-based devices, which is highly compromised by the hydrophilic nature of their surface that make them more prone to oxidation due to the attracted and confined water molecules and oxygen [51,52,63]. This fundamental limitation called for various solutions to be looked for, among which several involved chemical processes [51,64,65]. In this context, ion irradiation appears as a straightforward, flexible and highly scalable approach to overcome this challenge in the processing of MXene thin films for diverse applications [8,51,66,67].

For an in-depth understanding of the structural modifications induced at the flake scale and their impact on the electronic structure, advanced STEM-EELS characterizations were performed on the different samples. The corresponding spectra are given in Figures 3 and 4. They were normalized on the tail of the Ti L_2-edge at 469 eV in order to highlight possible chemical composition changes, and their energy positions were calibrated using the first peak of the C K-edge, set at 285 eV to allow for both a comparison of the relative energy shifts of the other peaks and a comparison with the literature [68–70]. For each sample, typically four different regions extracted from the films were analyzed: we did not notice any spatial inhomogeneities in terms of EELS signal for the pristine, S3, S8 and S15 samples (see SI part S4 for details), whereas for the largest fluence, *i.e.* sample S70, important inhomogeneities were observed. As a consequence, the spectra of the pristine, S3, S8 and S15 samples given in Figure 3 and 4 represent, for each edge, the average between the different investigated areas. For sample S70, the spectra of each one of the four investigated regions are plotted separately. The typical thicknesses of the investigated areas were estimated from the measured thickness to inelastic mean free path ratios (*i.e.* t/λ) deduced from the low loss spectra: they were typically ranging from $t/\lambda = 0.2$ to 0.4. Using the Malis expression for λ [71], which was shown to give rather good results for $Ti_3C_2T_z$ multilayers [72], the TEM samples thicknesses were then estimated to be between 30 and 60 nm depending on the investigated areas, *i.e.* corresponding to very significant portions of the thin films.

The EEL spectra were first used to characterize the evolution of the surface chemistry of the MXene flakes and the Cl $L_{2,3}$- and O K-edges recorded in different regions of the samples are given in Figure 3-a to c. Figure 3-c shows a comparison between the pristine sample O K-edge and the four spectra recorded on the different regions of S70, exhibiting different responses to irradiation. Due to the acquisition conditions, chosen to minimize the TEM-induced irradiation damages (see the methods section), the spectra are quite noisy: such low dose conditions were

however mandatory to avoid recording biased spectra. Focusing first on the Cl $L_{2,3}$-edges (Figure 3-a), one can clearly see that the main variation observed is a decrease of the overall intensity as a function of the fluence, with the pristine sample giving the highest intensity and the four areas of the S70 sample (labelled S70_1 to 4) the lowest ones. In region S70_4, the Cl signal has almost completely disappeared showing the almost complete sputtering of these surface groups in this area.

The evolutions are opposite at the O K-edge where the intensity, normalized to the Ti edge, is higher in the irradiated samples as compared to the pristine sample as can be seen in Figure 3-b. The comparison with the sample S70, given in Figure 3c, confirms this trend: the intensity under the O K-edge gets larger from zone 1 to 4, *i.e.* as a function of the Cl sputtering evidenced in Figure 3-a. For all samples, no sign of oxidation could be evidenced in the corresponding selected area electron diffraction - SAED - patterns (see SI – part S5). A quite direct explanation for the oxygen increase is that the desorption of the surface halogen groups (Cl but also F), which are less stable on MXene surfaces as evidenced from XPS measurements [73], gives new functionalization sites for oxygen atoms from the ambient atmosphere to passivate the Ti dangling bonds. In addition to the change in absolute intensity, one can see in Figure 3-b that the fine structures are also modified with a gradual blue shift of the first peak with increasing irradiation fluence, going up to ~1.5 eV for S15 (highlighted by green dashed lines in Figure 3-b), and accompanied by a broadening of this same peak. This denotes a change in the local environment of the surface oxygen atoms with the Cl/F desorption; it is again very consistent with XPS results showing a change in the 1s core level binding energy of the oxygen atoms with fluorine desorption [73,74].

EELS quantifications were performed on these spectra to determine the elemental ratios in the different samples. The results are presented in Figure 3-d where the evolution of the Ti/C and Ti/T (T ≡ O, F or Cl) ratios in the different samples, and normalized to the pristine one, are given. First of all, we observe almost no variation in the Ti/C ratio upon irradiation up to S15, which suggests that the integrity of the MXene skeleton is preserved, in agreement with the SAED patterns. As for S70, this ratio is much lower on average, with a large standard deviation, due to the important spatial inhomogeneities in terms of defects level in the studied regions. The relative Ti atom content decreases, suggesting a preferential sputtering of Ti for the highest irradiation fluence, similarly to what was reported by H. Pazniak *et al.* for Mn^+ implantation [48]. The evolution of the surface chemistry as a function of irradiation fluence was also examined by following the evolution of Ti/T ratios compared to those of the pristine sample.

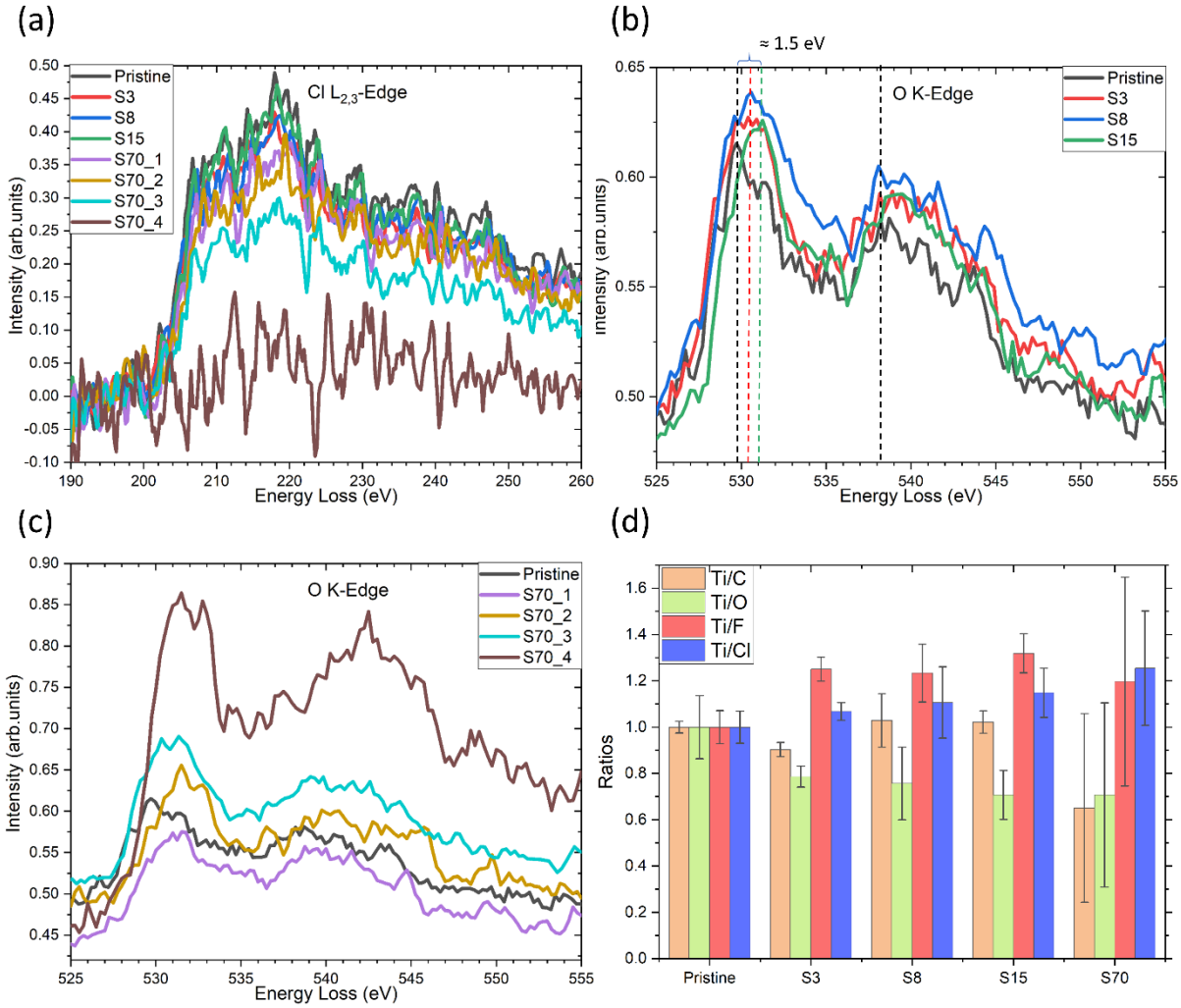

Figure 3: (a-c) Comparison of the Cl $L_{2,3}$ (a) and O K-edges (b,c) measured on the pristine and irradiated $Ti_3C_2T_z$ samples. Four S70 spectra are presented in (c) due to the spatial inhomogeneity of the irradiation damages observed in this sample. All spectra were normalized to the corresponding titanium intensity and aligned in energy using the C K-edge as an internal reference. The O K-edges were not background subtracted due to their superposition to the Ti $L_{2,3}$-edge, which prevents the use of standard background models. (d) EELS quantification results of the Ti/C, Ti/O, Ti/F and Ti/Cl ratios and determined from the Cl $L_{2,3}$, C K, Ti $L_{2,3}$, O K and F K-edges for the pristine and irradiated samples. The relative evolutions of the atomic concentration ratios, normalized to the pristine sample, are given.

The Ti/O ratio decreases as the irradiation fluence increases, confirming an increase of the oxygen content. Conversely, the Ti/F and Ti/Cl ratios increase, confirming a decrease in F and Cl terminations. Given that the Ti/C ratio indicates a stable Ti content for all fluences except for S70, these results confirm an irradiation-induced partial sputtering of the functional groups, which are then replaced by O atoms once the sample is exposed to ambient air.

In order to get insights into the structural modifications induced in the core of the MXene layers, *i.e.* the Ti_3C_2 skeleton, we now focus on the C K and Ti $L_{2,3}$-edges recorded in the different films. In Figure 4-a, are presented the C K-edges representative of the different samples, from pristine to S15 (see SI – part S6 for Ti-$L_{2,3}$ edges). These spectra are compared to that of the

pristine sample. As shown in Figure 4-b, and similarly to the T-groups, the C K-edges recorded on sample S70 exhibit very different features depending on the region where they were recorded. Focusing on Figure 4-a, the intensity ratio between peak A and peak B is markedly modified upon irradiation. According to first principles simulations by Bilyk *et al.* [54], these two peaks carry very different structural information: peak A is highly sensitive to surface perturbations on the MXene layers, while peak B is much more sensitive to the structural disorder within the Ti_3C_2 layer. In addition, peak A corresponds to the mixing of the unoccupied C-*p* states with the Ti-*d* states, which make it highly sensitive to changes in the Ti-*d* bands driving the electronic properties of $Ti_3C_2T_z$ layers. The change in the intensity of peak A thus reveals surface modifications, in agreement with the changes observed on the functional groups discussed previously (see Figure 3-d). In addition, Figure 4b also clearly shows important changes at the C K-edge for sample S70, with again different results as a function of the investigated region. In particular, for region S70_4, the C K-edge is strongly modified with a significant intensity increase revealing the titanium sputtering. In addition, the fine structure also clearly changes towards more sp^2-like bonding. This is again consistent with the loss of the titanium octahedral sites due to sputtering.

In order to provide a more quantitative analysis, the evolution of the peaks broadening in these spectra were finely analyzed by fitting the first two peaks of the C K-edges with two Gaussian functions and the Ti L_2-edge with a Lorentzian function (further details are given in the SI – part S7). Figure 3-c shows the full width at half maximum (FWHM) of peak B in the C K-edge as a function of the irradiation fluence, data for the pristine sample is given for comparison. The values obtained for S3 fall within the error bars of the pristine sample, indicating little to no change caused by irradiation. However, starting from S8, the peak B broadening shows monotonous increase with the irradiation fluence. According to the conclusions of T. Bilyk *et. al.* [54] this broadening evidences a gradual increase of the amount of defects inside the core of the $Ti_3C_2T_z$ layers. Although the precise nature of these defects is not here elucidated, the smooth evolution of the broadening of peak B as a function of the fluence clearly highlights the possibility to finely tune the defects density in MXene layers, which is a necessary step towards defect engineering in these 2D materials. In this context, ion irradiation appears as a very flexible and controllable approach, especially when compared to standard chemical exfoliation protocols, with important expected benefits in terms of properties (*e.g.*, gas permeation, sensing, electrocatalysis) [41,43–45,75].

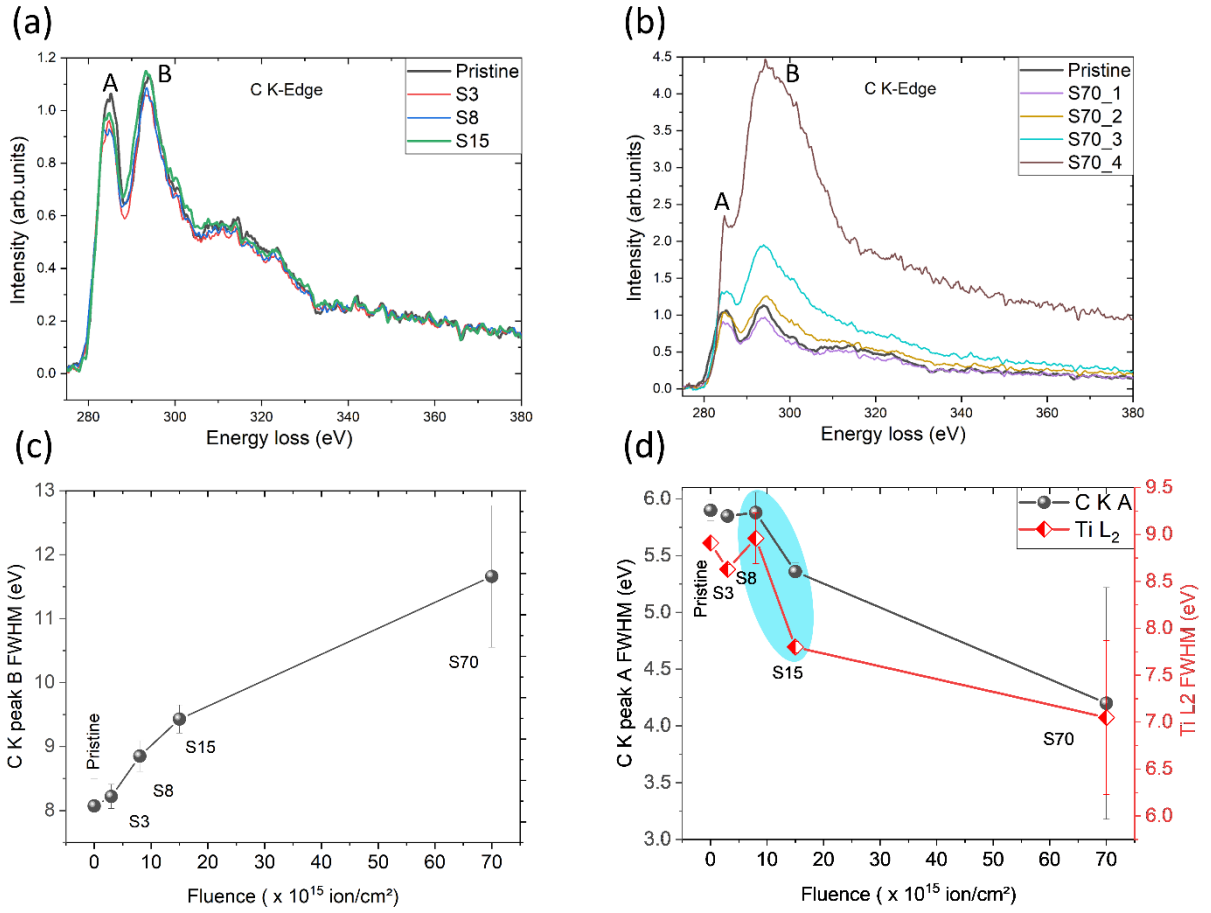

Figure 4: (a-b) Comparison between the C K-edge EEL spectra recorded in the pristine and irradiated $Ti_3C_2T_z$ samples. Four S70 spectra are presented in (b) to highlight the different levels of irradiation damage observed in the different regions of the sample. (c) C K-edge peak B full width at half maximum (FWHM) obtained from peak fitting as a function of the irradiation fluence. (d) C K-edge peak A and Ti-L_2-edge peaks FWHM obtained from peak fitting as a function of the irradiation fluence.

Very complementarily, Figure 4-d presents, as a function of the irradiation fluence, the evolution of the FWHM of the C K-edge peak A and Ti L_2-edge, as deduced from the fits presented in Figure S7 of the SI. A striking correlation is observed between the evolution of the broadening of these two peaks, with almost no evolution up to S8 and a significant decrease after S15 (highlighted in blue in Figure 4-d). Since the Ti $L_{2,3}$-edge is primary due to the excitation of the Ti 2*p* electrons in the empty Ti-*d* states, the modification of the Ti L_2-edge reflects significant changes in the Ti-*d* bands. That the evolution of the peak A at the C K-edge follows the same tendency is again very consistent with the conclusions of Bilyk *et. al.*[54]. These spectroscopic data thus show a significant perturbation of the Ti-*d* states for fluences greater than 8.10^{15} $He^+.cm^{-2}$. This point can be understood as revealing a threshold above which the electronic structure of $Ti_3C_2T_z$ layers becomes significantly affected by ion irradiation due to both surface modifications and defects formation within the MXene layers.

3.3 Impact on optical/electrical properties.

The effects of these He^+ irradiation induced structural modifications on the thin film properties have been investigated focusing on their optical and electrical properties, a major class of functional properties regarding optoelectronic applications for instance. Irradiated samples were characterized using a Variable Angle Spectroscopic Ellipsometer (VASE) to characterize their corresponding dielectric functions, and to measure their optical transmission (by using VASE in transmission intensity mode). The pristine sample presents a typical $Ti_3C_2T_z$ spectrum for both the imaginary (ε_2, Figure 5-a) and real (ε_1, Figure 5-b) parts of the dielectric function ε. The dielectric function of the pristine sample can be analyzed in terms of a minimal set of four contributions. First, a Drude term at low energy and responsible for the sharp increase (decrease) in ε_2 (ε_1): it describes the behavior of the conduction electrons responsible for the transport properties at the flake scale. At higher energy, three absorption peaks labelled P_1 to P_3 at 1.65 eV, 3.8 eV and 5.5 eV, respectively, can be observed in ε_2 (Figure 5-a). P_1 is responsible for the transmittance drop observed at 1.65 eV in Figure 6a which will be discussed later. It has been ascribed to a surface plasmon resonance in the $Ti_3C_2T_z$ layers [25,27,76]. Peaks P_2 and P_3 are responsible for the absorption in the UV (Figure 6-a) and correspond to interband transitions involving mixed C-*p*/Ti-*d* states in the valence band according to density functional theory calculations [77]. These last peaks are thus highly sensitive to the Ti_3C_2 skeleton of the MXene layers. The first change observed in the irradiated samples up to S15 is the shift of the Drude tail towards higher energies in ε_2 as the fluence increases. This is due to an increase of the Drude plasma frequency, characteristic of an increase of the charge carrier density as discussed below. The Drude contribution in sample S70 slightly decreases in energy compared to the preceding fluence. This can be related to preferential sputtering of the titanium atoms, as discussed before, reducing the electron density in the MXene flakes. The Drude contributions observed in the corresponding ε_1 spectra (see Figure 5-b) confirm the metallic nature of the samples, even for the highest fluence, and behave similarly to what was observed in the ε_2 spectra with a gradual attenuation of the spectral signatures as marked by arrows.

In order to quantify these changes, the optical models detailed in the supporting information (SI part S1) were applied to the pristine and irradiated samples. Charge carrier densities and mobilities of the conduction electron in the flakes were extracted. In Figure 5-c are presented the relative evolutions of the mean values and associated standard deviations obtained by applying these models to measurements performed on several (3 to 6) samples per fluence, as compared to the pristine sample. The pristine samples present an average charge carrier density of 1.4×10^{22} cm^{-3} and an average carrier mobility of 2.6 $cm^2.V^{-1}.s^{-1}$. These values are very

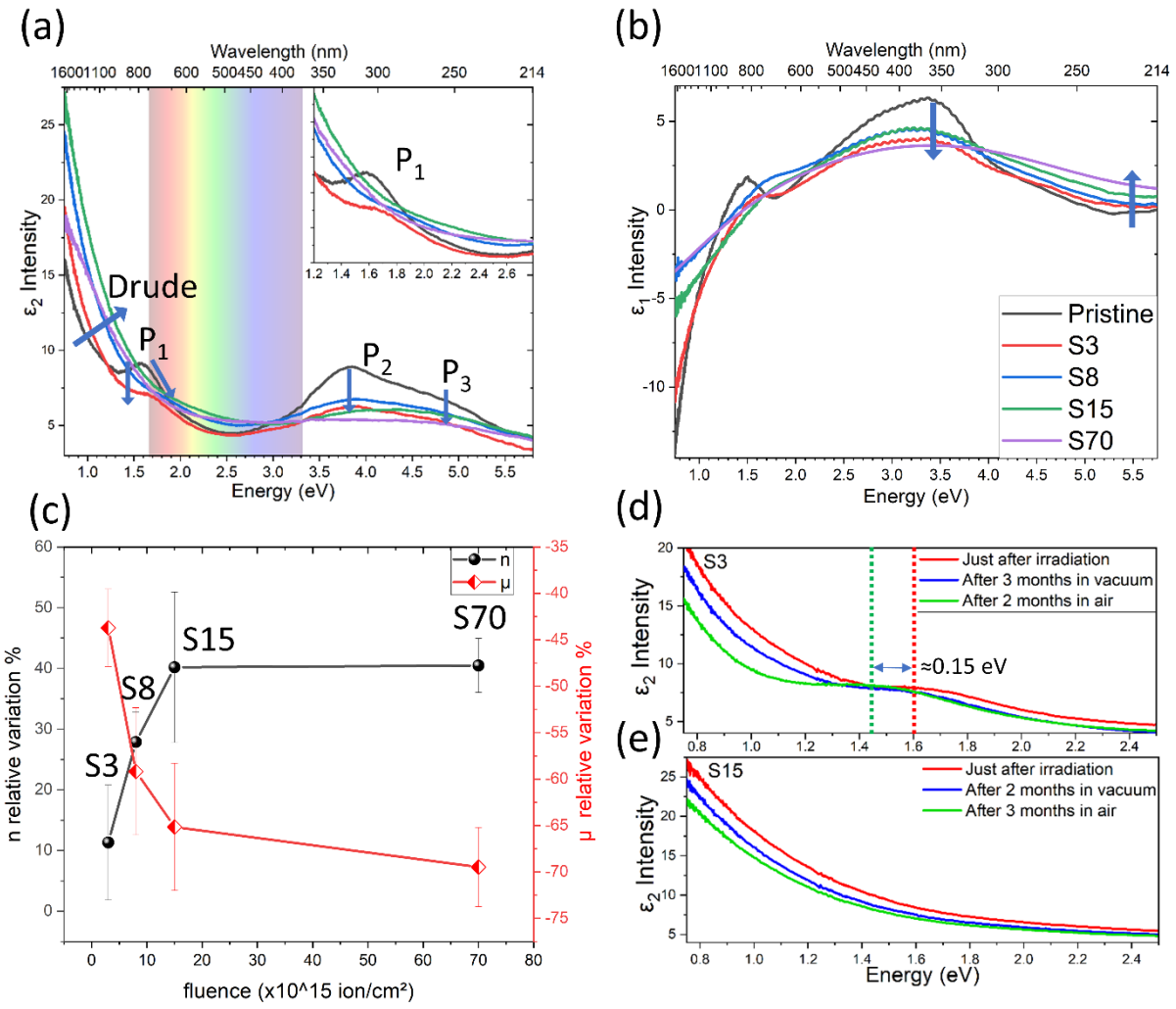

Figure 5: (a-b) VASE measurements of the imaginary (ε_2) and real (ε_1) parts of the dielectric function (respectively) of the pristine and irradiated samples. Inset in (a): magnification in the 1.2 to 2.8 eV energy range. Color codes relative to the different samples are given in (b). (c) Relative evolution, with respect to the pristine sample, of the charge carrier densities n and mobilities μ obtained from the optical models described in SI (part S1) as a function of the irradiation fluence. Concerning the optical and electrical properties, three to six different films were typically investigated for each fluence. (d-e) VASE spectra showing the aging of samples S3 and S15 (respectively) under low vacuum and then in air.

consistent with data reported in the literature [6,78]. On the one hand, the charge carrier density increases by up to 40% for the S15 and S70 sample as the irradiation fluence increases. Such an increase is fully consistent with the decrease of the interlayer spacing observed in the XRD measurements, given in Figure 2, resulting in an increase of the electron density at the film scale (see SI – part S8 showing the linear increase of the electron density as a function of the inverse of the interlayer spacing). On the other hand, the mobility decreases by up to 70% at the strongest fluence, indicating an impact of the defects introduced into the MXene layers forming the film, in agreement with EELS data analysis at the C K-edge (see Figure 4-c).

Focusing now on the peaks P_1 to P_3 at higher energy, the dielectric function also shows marked modifications. The P_1 peak is blue-shifted after the first irradiation and clearly attenuated. As

the ion fluence increases, this attenuation grows stronger, until the peak is completely eliminated (see the inset in Figure 5-a). Overall, the modification of the MXene flakes surfaces both in terms of chemistry but also in terms of the localization of the surface groups as discussed previously, appear as a very reasonable explanation for the strong modification of the P_1 peak, leading to its disappearance in the present case. In particular, this is consistent with the results of J.-K El-Demellawi *et al.* who showed that F desorption induced a strong damping of this peak at 1.65 eV using *in situ* STEM-EELS experiments [76]. It is also consistent with the fact that this signature is sensitive to the etching agent, and thus the surface chemistry of the layers [25]. The peaks P_2 and P_3 undergo similar changes, with an attenuated intensity after irradiation, accompanied by a broadening which can be directly related to the induced disorder within the MX core of the layers. Finally, aging tests were performed on these samples, and similarly to what was observed in XRD, optical experiments for samples S8, S15 and S70 are very stable. As examples, the imaginary parts of ε obtained for S3 and S15 are presented in Figure 5-d (see SI – part S9 for aging of samples S8 and S70). Focusing first on S15, one can clearly observe that the disappearance of the peak P_1 is very stable with time, be it after two months in low vacuum or three more months in air, confirming the good stability of the irradiation induced structural changes and corresponding impact on optical properties. On the contrary, and very consistently with the evolution observed in XRD, the optical properties of S3 slightly change with time showing that for such a small fluence the modifications of the MXene flakes are not stable. In particular, one can see that the peak P_1 is red shifted and broadened after two further months in air.

The observed modifications in the dielectric properties as analyzed from VASE measurements have direct impact on the corresponding properties, *i.e.* transmittance and resistivity of the films. The transmittance spectra of different pristine samples, given in Figure 6-a, show the typical features observed in solution processed $Ti_3C_2T_z$ thin films [78]. The transmissive range of the samples spans from 0.735 eV (*i.e.*, 1687 nm wavelength), the lower limit of our measurements, to about 3.5 eV (*i.e.*, 354 nm wavelength) with a maximum transmittance in the vis-near IR range of around 20% as expected for ~100 nm thick films (see SI – part S10)[22,78]. This maximum transmissive range is however strongly impacted by a prominent absorption peak at around 1.65 eV (*i.e.*, 751 nm wavelength, around the IR-vis limit), due to peak P_1 in ε_2 and reducing the transmittance by almost 40%. In the ultra-violet (UV) region (>3.5 eV), almost complete absorption is observed. It is important to mention that although the relative evolution of the transmittance is very reproducible, the absolute values obtained from these measurements are strongly dependent on the thicknesses of the samples as already pointed out by Dillon *et.*

al. [78]. This is further highlighted in SI (part S10) where a comparison between several pristine samples with varying film thicknesses, and prepared from the same initial MXene powder, is shown. Because of this thickness dependence, the discussion of the evolution of the optical properties upon irradiation for the different samples, which are of slightly different thicknesses, will be focused on relative evolutions rather than absolute values.

In order to better compare the different samples, the spectra of the pristine samples considered in Figure 6-a were normalized with respect to the integrated transmission over the IR-visible energy range (*i.e.*, the spectral range where they are transparent): the results given in Figure 6-a show that such normalization provides very similar transmission profiles for all thin films, evidencing that thickness dependency has been mostly removed. A similar procedure has been applied to the corresponding irradiated samples for direct visualization of the impact of irradiation, and the corresponding spectra are compared to a typical spectrum collected on a pristine film in Figure 6-b. These data show modifications of the thin films properties in well-defined energy ranges: (i) the absorption in the IR is gradually and significantly increased due to the increase in the charge carrier density and corresponding Drude plasma frequency, as discussed above; (ii) the transmission valley at the IR-vis limit is removed from S8 (above 8.10^{15} ions.cm^{-2}) due to the loss of the peak P_1, leading to a much more homogenous transmission profile in the visible range; and (iii) the transmittance in the UV is also significantly increased starting from S8. Figure 6-c gives a more quantitative picture of these modifications by showing the relative evolution, with respect to the corresponding pristine samples, of the integrated transmittance over different spectral ranges (*i.e.* IR, visible and visible+UV) of the irradiated films as a function of the fluence. This graph shows that the absorption in the IR range is increased by about 15% over the entire fluence range investigated here while the integrated transmission is barely affected by irradiation in the visible range. In the visible+UV range, the transmittance variation increases linearly with the fluence up to ~45% for S15 (considering the UV only leads to a much more important increase of ~500% since the transmittance of the pristine sample is very small). Overall these data show a well-defined role of ion irradiation depending on the investigated spectral range.

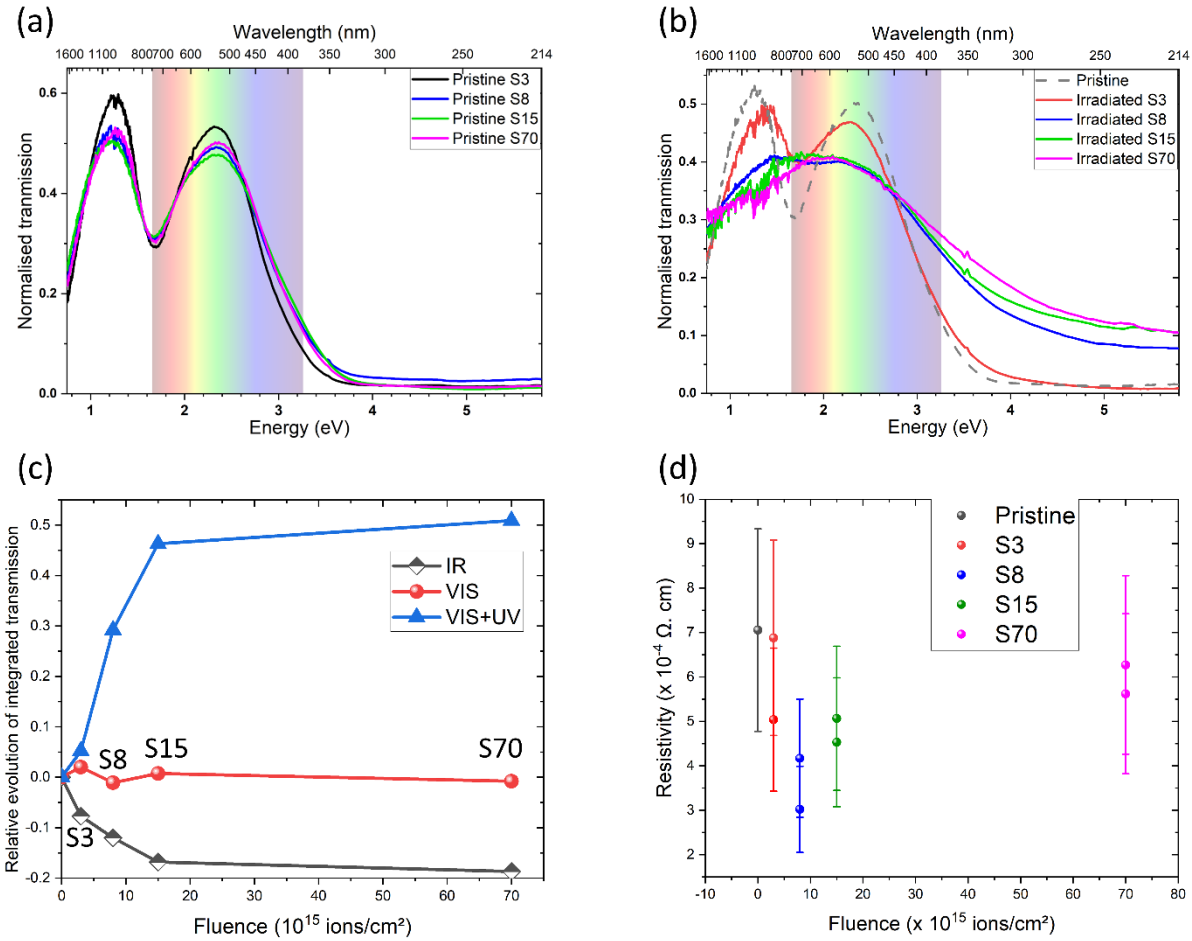

Figure 6: (a) Normalized transmission spectra of the different films before irradiation. The spectra have been normalized using the integrated area of each spectrum to mitigate sample thickness effects. (b) Normalized optical transmission spectroscopy measurements of the same samples as in (a) after irradiation with each fluence (full lines). These spectra are compared to a representative spectrum of pristine samples (dashed line). In both (a) and (b) the visible range is indicated by a light spectrum from 1.65 eV (751 nm) to 3.26 eV (380 nm). (c) Relative evolution of the integrated transmission for the irradiated samples, as compared to the corresponding pristine ones, and considering different spectral ranges: the infrared (IR: 0.73 eV – 1.65 eV - black), visible (VIS: 1.65 eV – 3.26 eV - red) and visible + ultraviolet (VIS+UV: 1.65 eV – 5.8 eV - blue). (d) Four points probe measurements of the resistivities of the thin films as a function of the irradiation fluence. For the irradiated samples, these measurements were performed after two months storage in low vacuum.

As far as electrical properties are concerned, it is important to notice that the samples keep a good conductivity after irradiation with a resistivity in the order of a few 10^{-4} Ω.cm even at the highest irradiation fluence (see Figure 6-d). Note that the measurements on the irradiated samples were performed after two months of storage in low vacuum: no degradation due to, *e.g.* oxidation, is observed. The fact that the good electrical properties are preserved can be straightforwardly understood from the structural and optical analysis performed in this study. The opposite evolution in the charge carrier properties (*i.e.* density and mobility) provide a good explanation to the relatively stable conductivity of the samples, where the drop of charge mobility is compensated by the increased carrier density, thus maintaining a good conductivity even for the strongest irradiation fluence. In addition, the reduction of the average interlayer

distance in the irradiated films, a critical parameter for MXene multilayers transport properties [61,79], improves the electrical contact between the MXene flakes, further compensating the effect of the structural defects at the flake scale and improving the conductivity. Having a closer look at Figure 6-d, one can notice a constant decrease of the resistivity from S0 to S8 before an increase for S15 and S70. This is consistent with EELS data clearly showing a significant alteration of the electronic structure of the MXene layers, involving a modification of the Ti *d*-bands (see Figure 4-d), starting at S15: this transition is consistent with the resistivity increase observed after S8 showing how modifications at the layer scale have an impact on the macroscopic properties of the films.

4. Conclusion

As a summary, ion irradiation has been demonstrated as an original strategy for the gradual and tunable structural engineering of MXene thin films, allowing to obtain tunable defect configurations. In particular, our results show that adjusting the ion beam fluence offers the possibility to play on almost all structural levels of MXene multilayers, ranging from the interlayer spacing and intercalated species, to the surface functionalization and finally the preferential sputtering of the transition metal layers of the MX core. These modifications, have a deep impact on the physico-chemical properties of the $Ti_3C_2T_z$ spin coated thin films investigated here. These modifications were rationalized in terms of chemical and electronic structure changes using state-of-the-art STEM-EELS analysis. In particular, the possibility to significantly reduce the hydration ability of these films, and corresponding aging issues, while preserving their transparency over the visible range with an extension in the UV, and improving electrical contacts between the MXene layers, is expected to be extremely beneficial for applications such as transparent conductive electrodes or charge transport layers for a large range of optoelectronic applications. The transition metal sputtering observed at higher fluences could also appear as very effective for diverse properties beyond those investigated here, where defect engineering in the transition metal layers is expected to play a pivotal role such as: catalysis [80], electrocatalysis [81], energy storage [82,83], sensing [84] or magnetism [85]. Given its versatility in designing new structure starting from pristine layers, ion irradiation is expected to provide original MXene layers, beyond those obtained from chemical approaches, thus enriching the properties and application range of this large class of 2D materials.

5. Supporting Information

Supporting Information is available from the Materials Today Physics Library or from the author.

6. Acknowledgements

This work partially pertains to the French Government program “Investissements d’Avenir” (LABEX INTERACTIFS, reference ANR-11-LABX-0017-01 and EUR INTREE, reference ANR-18-EURE-0010). This work has been partially supported by « Nouvelle Aquitaine » Region and by European Structural and Investment Funds (ERDF reference: P-2016-BAFE-94/95). Funding by the French Contrat Plan État-Région and the European Regional Development Fund of Pays de la Loire, the CIMEN Electron Microscopy Center in Nantes is greatly acknowledged. AB acknowledges the Nantes Université support for his Ph.D grant. Laurent Legras from the Gatan compagny is kindly acknowledged for his help in using the PIPS II apparatus. The authors wish to thank Marc Marteau for his assistance with the ion implantations, and Hadi Bahsoun for FIB-lamella preparations.

7. Conflict of interest

The authors declare no conflict of interest.

8. Data Availability Statement

The data that support the findings of this study are available from the corresponding author upon reasonable request.

9. References

[1] A. VahidMohammadi, J. Rosen, Y. Gogotsi, Science 372 (2021) eabf1581.
[2] A. H. Castro Neto, F. Guinea, N. M. R. Peres, K. S. Novoselov, A. K. Geim, Rev. Mod. Phys. 81 (2009) 109.
[3] K. F. Mak, J. Shan, Nature Photon 10 (2016) 216.
[4] K. Zhang, Y. Feng, F. Wang, Z. Yang, J. Wang, J. Mater. Chem. C 5 (2017) 11992.
[5] X. Jiang, A. V. Kuklin, A. Baev, Y. Ge, H. Ågren, H. Zhang, P. N. Prasad, Physics Reports 848 (2020) 1.
[6] K. Hantanasirisakul, Y. Gogotsi, Adv. Mater. 30 (2018) 1804779.
[7] A. Shayesteh Zeraati, S. A. Mirkhani, P. Sun, M. Naguib, P. V. Braun, U. Sundararaj, Nanoscale 13 (2021) 3572.
[8] S. Abdolhosseinzadeh, X. Jiang, H. Zhang, J. Qiu, C. (John) Zhang, Materials Today 48 (2021) 214.

[9] S. P. Sreenilayam, I. Ul Ahad, V. Nicolosi, D. Brabazon, Materials Today 2021, 43, 99.
[10] F. Shahzad, M. Alhabeb, C. B. Hatter, B. Anasori, S. Man Hong, C. M. Koo, Y. Gogotsi, Science 353 (2016) 1137.
[11] Y. Pei, X. Zhang, Z. Hui, J. Zhou, X. Huang, G. Sun, W. Huang, ACS Nano 15 (2021) 3996.
[12] D. Xiong, Y. Shi, H. Y. Yang, Materials Today 46 (2021) 183.
[13] J. Halim, M. R. Lukatskaya, K. M. Cook, J. Lu, C. R. Smith, L.-Å. Näslund, S. J. May, L. Hultman, Y. Gogotsi, P. Eklund, M. W. Barsoum, Chem. Mater. 26 (2014) 2374.
[14] M. Khazaei, M. Arai, T. Sasaki, A. Ranjbar, Y. Liang, S. Yunoki, Phys. Rev. B 92 (2015) 075411.
[15] X. Zhang, J. Shao, C. Yan, R. Qin, Z. Lu, H. Geng, T. Xu, L. Ju, Materials & Design 200 (2021) 109452.
[16] M. A. Saeed, A. Shahzad, K. Rasool, F. Mateen, J. Oh, J. W. Shim, Advanced Science 9 (2022) 2104743.
[17] L. Yang, C. Dall'Agnese, Y. Dall'Agnese, G. Chen, Y. Gao, Y. Sanehira, A. K. Jena, X. Wang, Y. Gogotsi, T. Miyasaka, Adv. Funct. Mater. 29 (2019) 1905694.
[18] S. Ahn, T. Han, K. Maleski, J. Song, Y. Kim, M. Park, H. Zhou, S. Yoo, Y. Gogotsi, T. Lee, Adv. Mater. 32 (2020) 2000919.
[19] J. Zhu, H. Wang, L. Ma, G. Zou, Nano Res. 14 (2021) 3416.
[20] K. Montazeri, M. Currie, L. Verger, P. Dianat, M. W. Barsoum, B. Nabet, Adv. Mater. 31 (2019) 1903271.
[21] L. Qin, J. Jiang, Q. Tao, C. Wang, I. Persson, M. Fahlman, P. O. Å. Persson, L. Hou, J. Rosen, F. Zhang, J. Mater. Chem. A (2020), 8, 5467.
[22] C. J. Zhang, B. Anasori, A. Seral-Ascaso, S.-H. Park, N. McEvoy, A. Shmeliov, G. S. Duesberg, J. N. Coleman, Y. Gogotsi, V. Nicolosi, Adv. Mater. 29 (2017) 1702678.
[23] M. Naguib, M. W. Barsoum, Y. Gogotsi, Adv. Mater. 33 (2021) 2170303.
[24] M. Sokol, V. Natu, S. Kota, M. W. Barsoum, Trends in Chemistry 1 (2019) 210.
[25] K. Maleski, C. E. Shuck, A. T. Fafarman, Y. Gogotsi, Adv. Optical Mater. 9 (2021) 2001563.
[26] B. Anasori, C. Shi, E. J. Moon, Y. Xie, C. A. Voigt, P. R. C. Kent, S. J. May, S. J. L. Billinge, M. W. Barsoum, Y. Gogotsi, Nanoscale Horiz. 1 (2016) 227.
[27] G. Valurouthu, K. Maleski, N. Kurra, M. Han, K. Hantanasirisakul, A. Sarycheva, Y. Gogotsi, Nanoscale 12 (2020) 14204.
[28] K. Hantanasirisakul, M. Alhabeb, A. Lipatov, K. Maleski, B. Anasori, P. Salles, C. Ieosakulrat, P. Pakawatpanurut, A. Sinitskii, S. J. May, Y. Gogotsi, Chem. Mater. 31 (2019) 2941.
[29] K. R. G. Lim, M. Shekhirev, B. C. Wyatt, B. Anasori, Y. Gogotsi, Z. W. Seh, Nat. Synth. 1 (2022) 601.
[30] J. L. Hart, K. Hantanasirisakul, A. C. Lang, B. Anasori, D. Pinto, Y. Pivak, J. T. van Omme, S. J. May, Y. Gogotsi, M. L. Taheri, Nat Commun 10 (2019) 522.
[31] V. Kamysbayev, A. S. Filatov, H. Hu, X. Rui, F. Lagunas, D. Wang, R. F. Klie, D. V. Talapin, Science 369 (2020) 979.
[32] M. M. Muhammed, J. H. Mokkath, Materials Today Chemistry 29 (2023) 101447.
[33] T. Su, X. Ma, J. Tong, H. Ji, Z. Qin, Z. Wu, J. Mater. Chem. A 10 (2022) 10265.
[34] J. Tang, H. Wan, L. Chang, B. Hu, S. Cui, Y. Chen, W. Chen, J. Hao, H. Tang, X. Wang, K. Wang, C. (John) Zhang, Q. Wen, X. Xiao, B. Xu, Advanced Optical Materials 10 (2022) 2200623.
[35] H. Jing, H. Yeo, B. Lyu, J. Ryou, S. Choi, J.-H. Park, B. H. Lee, Y.-H. Kim, S. Lee, ACS Nano 15 (2021) 1388.

[36] K. Hantanasirisakul, M. Zhao, P. Urbankowski, J. Halim, B. Anasori, S. Kota, C. E. Ren, M. W. Barsoum, Y. Gogotsi, Adv. Electron. Mater. 2 (2016) 1600050.
[37] M. Han, K. Maleski, C. E. Shuck, Y. Yang, J. T. Glazar, A. C. Foucher, K. Hantanasirisakul, A. Sarycheva, N. C. Frey, S. J. May, V. B. Shenoy, E. A. Stach, Y. Gogotsi, J. Am. Chem. Soc. 142 (2020) 19110.
[38] Z. M. Wong, T. L. Tan, A. J. K. Tieu, S.-W. Yang, G. Q. Xu, Chem. Mater. 31 (2019) 4124.
[39] M. Nastasi, J. W. Mayer, Ion Implantation and Synthesis of Materials, Springer Berlin Heidelberg, Berlin, Heidelberg, (2006).
[40] M. Schleberger, J. Kotakoski, Materials 11 (2018) 1885.
[41] Z. Li, F. Chen, Applied Physics Reviews 4 (2017) 011103.
[42] G. López-Polín, C. Gómez-Navarro, V. Parente, F. Guinea, M. I. Katsnelson, F. Pérez-Murano, J. Gómez-Herrero, Nature Phys. 11 (2015) 26.
[43] J. Liu, L. Jin, F. I. Allen, Y. Gao, P. Ci, F. Kang, J. Wu, Nano Lett. 21 (2021) 2183.
[44] P. D. Kaushik, M. Rodner, G. B. V. S. Lakshmi, I. G. Ivanov, G. Greczynski, J. Palisaitis, J. Eriksson, P. Solanki, A. Aziz, A. M. Siddiqui, R. Yakimova, M. Syväjärvi, G. R. Yazdi, Carbon 157 (2020) 169.
[45] L. Ma, Y. Tan, M. Ghorbani-Asl, R. Boettger, S. Kretschmer, S. Zhou, Z. Huang, A. V. Krasheninnikov, F. Chen, Nanoscale 9 (2017) 11027.
[46] Q. Yang, W. Wang, X. Li, Q. Li, M. Xun, L. Meng, Q. Tang, J. Xu, J Solid State Electrochem. 27 (2023) 1955.
[47] S. Patra, N. U. Kiran, P. Mane, B. Chakraborty, L. Besra, S. Chatterjee, S. Chatterjee, Surfaces and Interfaces 39 (2023) 102969.
[48] H. Pazniak, M. Benchakar, T. Bilyk, A. Liedl, Y. Busby, C. Noël, P. Chartier, S. Hurand, M. Marteau, L. Houssiau, R. Larciprete, P. Lacovig, D. Lizzit, E. Tosi, S. Lizzit, J. Pacaud, S. Célérier, V. Mauchamp, M.-L. David, ACS Nano 15 (2021) 4245.
[49] T. Li, G. Zhi, C. Chen, L. Zhang, S. Zhai, W. Dou, J. Wu, W. Hu, M. Zhou, ACS Appl. Nano Mater. 6 (2023) 3463.
[50] R. Ibragimova, Z.-P. Lv, H.-P. Komsa, Nanoscale Adv. 3 (2021) 1934.
[51] H. Zhou, S. J. Han, H. Lee, D. Zhang, M. Anayee, S. H. Jo, Y. Gogotsi, T. Lee, Advanced Materials 34 (2022) 2206377.
[52] T. Wu, P. R. C. Kent, Y. Gogotsi, D. Jiang, Chem. Mater. 34 (2022) 4975.
[53] M. Benchakar, L. Loupias, C. Garnero, T. Bilyk, C. Morais, C. Canaff, N. Guignard, S. Morisset, H. Pazniak, S. Hurand, P. Chartier, J. Pacaud, V. Mauchamp, M. W. Barsoum, A. Habrioux, S. Célérier, Applied Surface Science 530 (2020) 147209.
[54] T. Bilyk, M. Benchakar, M. Bugnet, L. Loupias, P. Chartier, H. Pazniak, M.-L. David, A. Habrioux, S. Celerier, J. Pacaud, V. Mauchamp, J. Phys. Chem. C 124 (2020) 27071.
[55] D. Magne, V. Mauchamp, S. Célérier, P. Chartier, T. Cabioc'h, Phys. Chem. Chem. Phys. 18 (2016) 30946.
[56] L. H. Karlsson, J. Birch, J. Halim, M. W. Barsoum, P. O. Å. Persson, Nano Lett. 15 (2015) 4955.
[57] M. Shekhirev, C. E. Shuck, A. Sarycheva, Y. Gogotsi, Progress in Materials Science 120 (2021) 100757.
[58] M. A. Hope, A. C. Forse, K. J. Griffith, M. R. Lukatskaya, M. Ghidiu, Y. Gogotsi, C. P. Grey, Phys. Chem. Chem. Phys. 18 (2016) 5099.
[59] F. Brette, D. Kourati, M. Paris, L. Loupias, S. Célérier, T. Cabioc'h, M. Deschamps, F. Boucher, V. Mauchamp, J. Am. Chem. Soc. 145 (2023) 4003.
[60] J. F. Ziegler, M. D. Ziegler, J. P. Biersack, Nuclear Instruments and Methods in Physics Research Section B: Beam Interactions with Materials and Atoms 268 (2010), 1818.

[61] S. Célérier, S. Hurand, C. Garnero, S. Morisset, M. Benchakar, A. Habrioux, P. Chartier, V. Mauchamp, N. Findling, B. Lanson, E. Ferrage, Chem. Mater. 31 (2019) 454.
[62] M. Ghidiu, J. Halim, S. Kota, D. Bish, Y. Gogotsi, M. W. Barsoum, Chem. Mater. 28 (2016) 3507.
[63] S. Huang, V. Natu, J. Tao, Y. Xia, V. N. Mochalin, M. W. Barsoum, J. Mater. Chem. A (2022), 10, 22016.
[64] X. Zhao, A. Vashisth, E. Prehn, W. Sun, S. A. Shah, T. Habib, Y. Chen, Z. Tan, J. L. Lutkenhaus, M. Radovic, M. J. Green, Matter 1 (2019) 513.
[65] W. Y. Chen, S.-N. Lai, C.-C. Yen, X. Jiang, D. Peroulis, L. A. Stanciu, ACS Nano 14 (2020) 11490.
[66] C. (John) Zhang, V. Nicolosi, Energy Storage Materials (2019), 16, 102.
[67] X. Fan, Adv. Funct. Mater. 31 (2021) 2009399.
[68] M. Magnuson, J.-P. Palmquist, M. Mattesini, S. Li, R. Ahuja, O. Eriksson, J. Emmerlich, O. Wilhelmsson, P. Eklund, H. Högberg, L. Hultman, U. Jansson, Phys. Rev. B 72 (2005) 245101.
[69] J. A. Brandes, G. D. Cody, D. Rumble, P. Haberstroh, S. Wirick, Y. Gelinas, Carbon 46 (2008) 1424.
[70] A. Tararan, A. Zobelli, A. M. Benito, W. K. Maser, O. Stéphan, Chem. Mater. 28 (2016) 3741.
[71] T. Malis, S. C. Cheng, R. F. Egerton, J. Elec. Microsc. Tech. 8 (1988) 193.
[72] T. Bilyk, H.-W. Hsiao, R. Yuan, M. Benchakar, A. Habrioux, S. Célérier, J.-M. Zuo, J. Pacaud, V. Mauchamp, 2D Mater. 9 (2022) 035017.
[73] I. Persson, L.-Å. Näslund, J. Halim, M. W. Barsoum, V. Darakchieva, J. Palisaitis, J. Rosen, P. O. Å. Persson, 2D Mater. 5 (2017) 015002.
[74] T. Schultz, N. C. Frey, K. Hantanasirisakul, S. Park, S. J. May, V. B. Shenoy, Y. Gogotsi, N. Koch, Chem. Mater. 31 (2019) 6590.
[75] C. Sun, P. Wang, H. Wang, C. Xu, J. Zhu, Y. Liang, Y. Su, Y. Jiang, W. Wu, E. Fu, G. Zou, Nano Res. 12 (2019) 1613.
[76] J. K. El-Demellawi, S. Lopatin, J. Yin, O. F. Mohammed, H. N. Alshareef, ACS Nano 12 (2018) 8485.
[77] D. Magne, V. Mauchamp, S. Célérier, P. Chartier, T. Cabioc'h, Phys. Rev. B 91 (2015) 201409.
[78] A. D. Dillon, M. J. Ghidiu, A. L. Krick, J. Griggs, S. J. May, Y. Gogotsi, M. W. Barsoum, A. T. Fafarman, Adv. Funct. Mater. 26 (2016) 4162.
[79] J. Halim, E. J. Moon, P. Eklund, J. Rosen, M. W. Barsoum, T. Ouisse, Phys. Rev. B 98 (2018) 104202.
[80] D. Zhao, Z. Chen, W. Yang, S. Liu, X. Zhang, Y. Yu, W.-C. Cheong, L. Zheng, F. Ren, G. Ying, X. Cao, D. Wang, Q. Peng, G. Wang, C. Chen, J. Am. Chem. Soc. 141 (2019) 4086.
[81] J. Gan, F. Li, Q. Tang, J. Phys. Chem. Lett. 12 (2021) 4805.
[82] X. Wang, J. Chen, D. Wang, Z. Mao, ACS Appl. Energy Mater. 4 (2021) 10280.
[83] N. Chen, Y. Zhou, S. Zhang, H. Huang, C. (John) Zhang, X. Zheng, X. Chu, H. Zhang, W. Yang, J. Chen, Nano Energy 85 (2021) 106007.
[84] Z. Yang, H. Zou, Y. Zhang, F. Liu, J. Wang, S. Lv, L. Jiang, C. Wang, X. Yan, P. Sun, L. Zhang, Y. Duan, G. Lu, Adv. Funct. Materials 32 (2022) 2108959.
[85] K. Zhang, M. Di, L. Fu, Y. Deng, Y. Du, N. Tang, Carbon 157 (2020) 90.